Plasmon-enhanced luminescence near noble-metal nanospheres: Comparison of exact theory and an improved Gersten and Nitzan model

H. Mertens,* A. F. Koenderink, and A. Polman
Center for Nanophotonics, FOM Institute for Atomic and Molecular Physics, Kruislaan 407, 1098 SJ Amsterdam, The Netherlands
(Received 18 December 2006; revised manuscript received 15 May 2007; published 21 September 2007)

We present a theoretical study of the modifications of the radiative and nonradiative decay rates of an optical emitter in close proximity to a noble-metal nanosphere, based on exact electrodynamical theory. We show that the optimal nanosphere diameter for luminescence quantum efficiency enhancement associated with resonant coupling to plasmon modes is in the range of 30–110 nm, depending on the material properties. The optimal diameter is found to be a trade-off between (1) emitter-plasmon coupling, which is most effective for small spheres, and (2) the outcoupling of plasmons into radiation, which is most efficient for large spheres. In addition, we show that the well-known Gersten and Nitzan model does not describe the existence of a finite optimal diameter unless the model is extended with the correction factor for radiation damping. With this correction and a correction for dynamic depolarization, the mathematically simpler Gersten and Nitzan model provides a reasonably accurate approximation of the decay rate modifications associated with coupling to the dipole plasmon mode. We anticipate that the Gersten and Nitzan model in the form that we validate in this paper for spheres will allow the analytical investigation of the influence of shape anisotropy on plasmon-enhanced luminescence.

DOI: 10.1103/PhysRevB.76.115123 PACS number(s): 78.20.Bh, 73.20.Mf, 32.50.+d

I. INTRODUCTION

During the last decade, there has been a strong revival in experimental efforts to control spontaneous emission dynamics by metal nanostructures.[1–5] In particular, the recent advances in nano-optics,[3–5] which allow for experiments on single molecules interacting with well-defined metal nanostructures, often referred to as nanoantennas,[6,7] serve as a strong impetus for this development. These single-molecule experiments, which focus on the resonant coupling of emitters with plasmon modes, i.e., collective conduction electron oscillations in the metal, have led to the observation of photoluminescence enhancement and quenching depending on the distance between emitter and metal,[4] with concomitant changes in excited state lifetime.[3,5] In addition to these fundamental breakthroughs, the recent progress in nanotechnology enables the introduction of plasmon-enhanced luminescence in various applications, e.g., for enhancing the brightness of technologically important light emitters[8,9] or for enhancing emission in a polarization-selective way.[10] Besides, plasmon-enhanced luminescence has great potential for sensing applications[11] and for improving the light-harvesting capabilities of solar cells.

With the ongoing interest in the electromagnetic interaction between emitters and metal nanostructures, there is a growing demand for theoretical studies that provide insight on the physical factors that determine the performance of nanoantennas.[12–17] The need for such investigations is emphasized by the fact that, due to both the absorptive nature of metals and the high confinement of plasmonic modes, only in a limited part of the extensive parameter space can metal nanostructures provide exceptional improvements to the radiative properties of emitters.

In this paper, we present an extensive survey, based on an exact electrodynamical theory,[18–20] of the modifications of the radiative and nonradiative decay rates of an emitter in close proximity to a metal sphere. We focus on the enhancement of the quantum efficiency of a low-quantum-efficiency emitter by resonant coupling to the plasmon modes of the sphere. We explain the dependencies of the quantum efficiency on emitter-metal separation and on sphere size based on the scattering and absorption properties of the plasmon modes of the sphere. This approach provides physical insight on the extent to which radiative and nonradiative decay rate enhancements are intrinsically linked, or can be separated by design. By comparing results for Ag and Au to the results for an ideal Drude metal, we also determine which of the observed trends are intrinsic to a free-electron response and which are related to interband transitions in the metals. Furthermore, we address the strong influence of dipole emitter orientation relative to the sphere on plasmon-enhanced luminescence.

In the second part of the paper, we compare the exact electrodynamical theory with the results from the model by Gersten and Nitzan[21,22] (GN): a quasistatic model in which retardation effects are treated as perturbations. The advantage of the GN model is that it can be generalized to spheroids based on an expansion in terms of an orthogonal set of eigenfunctions, so that shape-induced shifts of the plasmon resonance frequencies and shape-induced changes in field intensities can be accounted for. Such an expansion is not known for exact electrodynamical theory.[23] The goal of our comparison is to validate such an approach based on the GN model. In this paper, we conclude that it is necessary to improve the GN model to account for radiation damping[24] and dynamic depolarization[25] according to Wokaun and coworkers. These corrections have previously been studied in the framework of far-field scattering,[26] but not in the context of spontaneous emission. We demonstrate that the improved GN model can be applied over a substantially larger particle-size range than the original version.[27] In particular, we show that the improved GN model, in contrast to the original ver-

sion, does describe the existence of a finite optimal diameter for plasmon-enhanced luminescence, which is consistent with the exact electrodynamical theory.[28]

The paper is organized as follows. In Sec. II, we summarize the two theoretical approaches that we adopt. In Sec. III, we discuss the influence of the separation between a low-quantum-efficiency emitter and a Ag sphere on the radiative and nonradiative decay rates, and thus on the quantum efficiency, of the emitter. In Sec. IV, we focus on the dependence of the quantum efficiency enhancement on the sphere size. In Sec. V, we compare the exact electrodynamical theory to both the original and the improved GN models. Finally, conclusions are presented in Sec. VI.

II. METHODS

In this section, we first summarize the exact electrodynamical description of spontaneous emission dynamics near a metal nanosphere as developed by Ruppin[18] and by Kim *et al.*[19] After that, we discuss the description of spontaneous emission dynamics based on the model by Gersten and Nitzan.[21,22]

The modification of spontaneous emission can be described classically.[29] The excited state decay rate, which in the presence of absorbing dielectrics consists of radiative and nonradiative components, is proportional to the work $W \propto \mathbf{j}\cdot\mathbf{E}$ that the field $\mathbf{E}$ generated by a current source $\mathbf{j}(\mathbf{r},t)$ does on the source itself.[30] The excited state decay rate in the presence of a metal sphere, normalized to the rate in a bulk dielectric, is obtained by comparing the work W done on a source in the presence of the sphere to the work W_0 done on the same current source in the bulk dielectric. The analytical expressions for this decay rate, which can be derived from the Green function[20] for a sphere, are given in the Appendix. The modification of the radiative decay rate is found by comparing the energy flux through a surface that encloses both source and sphere to the radiated power of the same source dipole in the bulk dielectric (see the Appendix).[18,19] The nonradiative decay rate due to dissipation in the absorbing sphere is obtained by taking the difference between the excited state decay rate and the radiative decay rate. Note that the nonradiative decay rate, and thus also the excited state decay rate of a luminescent species, may contain additional components, e.g., due to Auger processes, that are not described by the local electromagnetic theory. Within the context of the exact electrodynamical theory, also the angular emission distribution of a source dipole in proximity to a metal sphere is analyzed. Such distributions are calculated from an expansion of the electric dyadic Green function in terms of vector spherical harmonics.[20]

In the GN model,[21,22] which is the second calculation method that we adopt, the modifications of the radiative and nonradiative decay rates are calculated in a two-step approach. In the first step, the electromagnetic interaction between source dipole and sphere is analyzed using the quasistatic approximation.[31] In this approximation, all dimensions are assumed to be much smaller than the wavelength of light, so that retardation can be neglected. The analysis can then be based on electrostatics. The solution for the electrostatic potential is a superposition of the source dipole potential and the induced multipoles of the sphere.[22] Note that for small particles, a dipole source at short distance induces higher-order multipoles because of the strong gradients in the near field of the source. This is different for plane-wave illumination of such particles, which can only excite dipole modes.

In the second step, an effective dipole moment of the coupled system is identified. This effective dipole moment, which comprises a vectorial superposition of the source dipole moment and the induced dipole moment, is used to calculate the radiated power. By normalization to the power radiated by an uncoupled source with identical dipole moment, the modification of the radiative decay rate is obtained. The induced nonradiative decay rate is determined by calculating the power that is dissipated in the sphere using the Joule heating law.[32] Since the electric field in the sphere is a superposition of all multipole modes, all these modes contribute to the nonradiative decay rate, whereas only the dipole mode is assumed to affect the radiative decay rate. This assumption is not made in the approach that relies on the exact electrodynamical theory. In Sec. V, it is discussed for what metal sphere sizes the assumption is justified. We find that under particular conditions, higher-order modes can enhance the radiative decay rate as well.

In the present paper, we have improved the first step of the GN model by adding two corrections that have been introduced successfully for improving the quasistatic description of scattering. These corrections take into account that the magnitude of the induced dipole moment is not only limited by absorption, but also by radiation losses.[24] Besides, the redshift of the dipole plasmon resonance caused by retardation of the depolarization field due to the finite dimensions of the sphere[25] is implemented as well. Both these corrections to the original GN model are taken into account by an effective nanoparticle polarizability that differs from the electrostatic polarizability by a correction factor.[33] Neither of these two corrections has been taken into account in a previous comparison of the GN model for spontaneous emission and the exact electrodynamical theory,[27] although the first correction is essential for satisfying the optical theorem.

III. DECAY RATE MODIFICATIONS VERSUS EMITTER-SPHERE SEPARATION

We consider the modifications of the radiative decay rate Γ_R, the nonradiative decay rate Γ_{NR}, and the quantum efficiency $\eta=\Gamma_R/(\Gamma_R+\Gamma_{\mathrm{NR}})$ of an emitter that is embedded in a homogeneous dielectric with a refractive index of 1.3 and which has an internal luminescence quantum efficiency of 1% in the absence of the sphere. The choice for the relatively low quantum efficiency enables the illustration of some important aspects associated with the coupling of an emitter to the plasmon modes of a metal sphere. In this section, the emitter is positioned near a Ag sphere with a diameter of 60 nm. The optical data of Ag are taken from Palik,[34] and the source dipole orientation is averaged over all solid angles (see the Appendix), which is representative for experiments on collections of atoms with randomly oriented transition dipole moments. The influence of specific dipole orientations

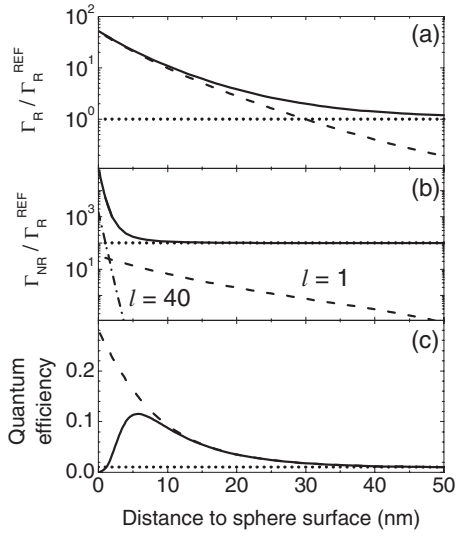

FIG. 1. (a) Radiative decay rate of a dipole emitter, the orientation of which is averaged over all solid angles, versus the distance to the surface of a 60-nm-diameter Ag sphere (solid line), the contribution to the radiative decay rate due to coupling with the dipole plasmon mode (dashed line), and the radiative decay rate in the absence of the sphere (dotted line). (b) Nonradiative decay rate versus distance to the sphere surface when taking into account coupling to all modes up to $l=60$ (solid line), the contributions to the nonradiative decay rate due to the $l=1$ or dipole mode (dashed line) and due to the $l=40$ mode (dash-dotted line), and the nonradiative decay rate in the absence of the sphere (dotted line). The decay rates in both (a) and (b) are normalized to the radiative decay rate in the absence of the sphere. If $l \to \infty$, then the nonradiative decay rate would diverge for $d \to 0$. (c) Luminescence quantum efficiency versus distance to the sphere surface when taking into account coupling to all modes up to $l=60$ (solid line) and when taking into account coupling to the dipole plasmon mode only (dashed line), and the quantum efficiency in the absence of the sphere (dotted line). The quantum efficiency of the emitter in the absence of the sphere is 1%, the refractive index of the embedding medium is 1.3, and the emission wavelength is 433 nm. Calculation method: exact electrodynamical theory.

on the decay rate enhancements will be discussed later. The emission wavelength ($\lambda_{em}=433$ nm) is chosen such that the emission is resonant with the dipole plasmon mode of the sphere. All results in this section were calculated from the exact electrodynamical theory, as described in Sec. II.

Figure 1(a) shows the radiative decay rate, normalized to the radiative decay rate in the absence of the sphere, as a function of the distance to the sphere surface (solid line). At a distance of 0 nm, the radiative decay rate is 50 times larger than in the absence of the sphere, and it drops off to a factor of 2 in about 30 nm. The radiative decay rate is composed of two contributions: the radiative decay rate of the emitter in the absence of the sphere (dotted line) and the contribution due to the presence of the sphere (dashed line), which can be fully attributed to coupling to the dipole mode. An explanation of the decomposition of the decay rates into various contributions can be found in the Appendix.

Figure 1(b) shows a similar plot for the nonradiative decay rate. The solid line represents the total nonradiative decay rate, which is composed of two types of contributions. The dotted line is the sphere-independent contribution, which is 99 times larger than its radiative counterpart because of the choice for a quantum efficiency of 1% in the absence of the sphere. The dashed lines are contributions due to coupling to two representative plasmon modes with different angular mode numbers l: $l=1$ (dipole) and $l=40$. The $l=1$ mode contributes to the nonradiative decay rate at relatively large distances, whereas the $l=40$ mode is only significant at very small distances. In the calculation of the total nonradiative decay rate (solid line), coupling to all plasmon modes up to $l=60$ was taken into account. Including these higher-order modes results in convergence at emitter-metal separations down to 1 nm. In the limit of the separation going to 0, the nonradiative decay rate diverges within a local description of the nanosphere material with a complex dielectric constant. This divergence is not described by a finite number of angular mode numbers l. In this paper, we do not focus our analysis on emitter-sphere separations of 1 nm or smaller, since under those conditions electronic energy transfer between emitter and metal needs to be taken into account, which is beyond the scope of all purely electrodynamic models presented in this paper.

Figure 1(c) shows the quantum efficiency η as a function of emitter-nanoparticle separation. The dashed line shows the behavior if only coupling to the dipole mode is taken into account. The trend is a monotonic increase in quantum efficiency upon decreasing the emitter-nanoparticle separation. If all modes up to $l=60$ are taken into account (solid line), a similar trend is found down to a separation of 10 nm, but a strong decrease is observed when the separation is reduced further. This result demonstrates that quenching at short distances follows simply from coupling to nonresonant higher-order plasmon modes. Because these modes do not efficiently couple to the far field, they can be considered as dark modes.[35] Coupling to these modes hence always reduces the quantum efficiency. We conclude that the quenching at short emitter-metal separations can be described without invoking nonlocal phenomena, such as the anomalous skin effect.[36]

More quantitatively, Fig. 1(c) shows that, at separations of 5–10 nm, the quantum efficiency is enhanced by an order of magnitude. At a separation of 6 nm, the 11-fold quantum efficiency enhancement is the combined effect of 19-fold radiative decay rate enhancement and a 1.5-fold nonradiative decay rate enhancement. If the quantum efficiency in the absence of the sphere is 0.1% instead of 1%, then the maximum quantum efficiency would be 2.3%, which corresponds to an enhancement of a factor of 23. Conversely, if the quantum efficiency in the absence of the sphere is 10%, then the maximum quantum efficiency would be 32%, which corresponds to an enhancement of only a factor of 3.2. These results illustrate how the numerical values of the calculated quantum efficiencies depend on the choice of the quantum efficiency in the absence of the sphere. In the remainder of this paper, we limit ourselves to an emitter with a quantum efficiency of 1% in the absence of the sphere. We use this value to explore the trends in quantum efficiency enhancement upon changing the geometry.

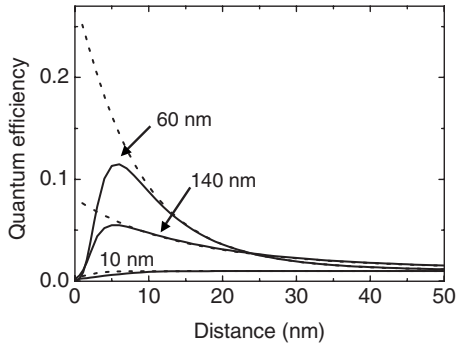

FIG. 2. Quantum efficiency of a dipole emitter, the orientation of which is averaged over all solid angles, versus distance to the surface of a Ag sphere for three sphere diameters: 10, 60, and 140 nm, when taking into account coupling to all modes up to $l=80$ (solid lines) and when taking into account coupling to the dipole mode only (dashed lines). The refractive index of the embedding medium is 1.3 and the quantum efficiency of the emitter in the absence of the sphere is 1%. The calculations were done at the wavelength of maximum radiative decay rate enhancement for each diameter. Calculation method: exact electrodynamical theory.

IV. QUANTUM EFFICIENCY ENHANCEMENT VERSUS SPHERE DIAMETER

A. Optimum size for quantum efficiency enhancement

The magnitude of the quantum efficiency enhancement due to resonant coupling to plasmon modes depends strongly on sphere diameter. Figure 2 shows the quantum efficiency of a dipole emitter, the orientation of which is averaged over all solid angles, as a function of the distance to a Ag sphere, for three sphere diameters: 10, 60, and 140 nm. The emission wavelength is adjusted for every diameter in order to match the size-dependent dipole resonance at 397, 433, and 683 nm, for diameters of 10, 60, and 140 nm, respectively. For all three diameters, two curves are plotted: one for which only coupling to the dipole mode is taken into account (dashed lines) and one for which coupling to all modes up to $l=80$ is taken into account (solid lines).

Figure 2 shows that the highest quantum efficiency enhancement is found for the intermediate diameter (60 nm). By comparing the solid and dashed lines in the figure, it can be concluded that the size dependence of the maximum quantum efficiency enhancement is due to the electromagnetic properties of the radiative dipole mode only, and that it does not relate to the dark higher-order modes, which are responsible for the drop in quantum efficiency at short distances.

To trace out the dependence on sphere size, Fig. 3(a) displays the wavelength of maximum radiative decay rate enhancement associated with coupling to the dipole mode versus sphere diameter for a dipole emitter, the orientation of which is averaged over all solid angles for three sphere materials: Ag, Au, and a Drude metal. The optical data for Ag and Au were taken from Ref. 34 and are shown in Fig. 4. The parameters for the Drude metal, i.e., plasma frequency (1.2×10^{16} rad/s) and electron relaxation frequency (9×10^{13} rad/s), were obtained from a fit to the data for Ag in the infrared part of the spectrum, where the Drude model provides an accurate description of the electromagnetic response of Ag. Figure 3(a) shows a redshift of the wavelength of maximum radiative decay rate enhancement with increasing diameter for all three materials. This redshift is directly related to the dipole resonance redshift for increasing size, which is mainly attributed to retardation of the depolarization field across the sphere diameter.[25] We note that the wavelength of maximum radiative decay rate enhancement is

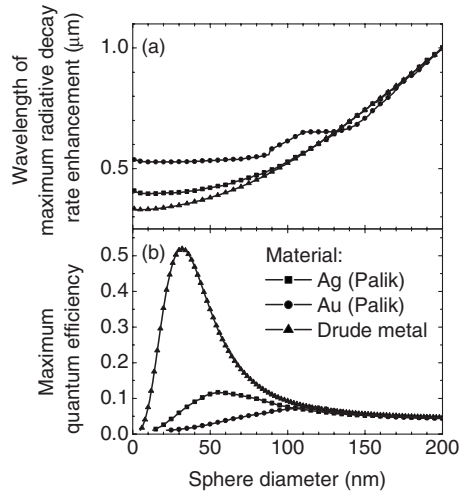

FIG. 3. (a) Wavelength of maximum radiative decay rate enhancement associated with coupling to the dipole plasmon mode versus sphere diameter for a dipole emitter, the orientation of which is averaged over all solid angles, positioned in close proximity to a sphere, plotted for three sphere materials: Ag, Au, and a Drude-model fit for Ag. (b) Maximum quantum efficiency versus sphere diameter at the wavelength shown in (a) for the same three materials. The maximum quantum efficiency was found by varying the emitter-sphere separation (see text). The refractive index of the embedding medium is 1.3 and the quantum efficiency of the emitter in the absence of the sphere is 1%. Calculation method: exact electrodynamical theory.

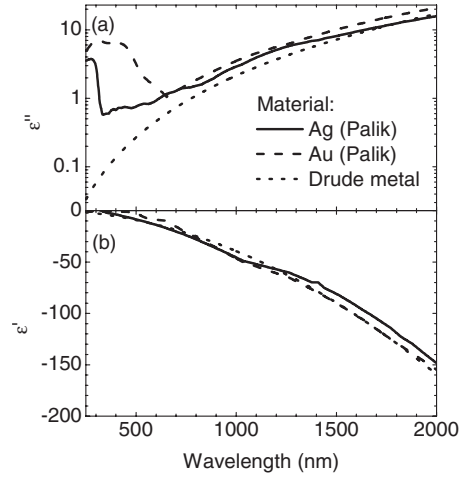

FIG. 4. (a) Imaginary part, plotted on a logarithmic scale, and (b) real part, plotted on a linear scale, of the dielectric functions of the three sphere materials used in the calculations.

independent of emitter-sphere separation for the subwavelength distances we are interested in.

Figure 3(b) shows the maximum quantum efficiency calculated at the wavelength shown in Fig. 3(a), also taking into account coupling to higher-order modes (see the Appendix). The maximum quantum efficiency refers to the maximum values in quantum-efficiency-versus-distance plots like Fig. 2, and thus represent different (optimized) emitter-sphere separations, ranging from 3 to 10 nm. Figure 3(b) illustrates that for all three materials an optimal diameter for quantum efficiency enhancement can be identified. That this is also possible for the Drude metal implies that the existence of such an optimal diameter can be described based on a purely free-electron response for the metal.

Despite the qualitative correspondence between the three curves of Fig. 3(b), large numerical differences are found for the three materials. The optimal diameter is 30 nm for the Drude metal, 55 nm for Ag, and 110 nm for Au. Moreover, the maximum quantum efficiency is 52% for the Drude metal, 11% for Ag, and only 7% for Au. These differences are related to the fact that the imaginary parts of the dielectric functions of Ag and Au are much higher than that of an ideal Drude metal, as is clearly visible in Fig. 4, for wavelengths below 600 nm. The difference is due to interband transitions.[36] Since the Drude model fits the dielectric functions of both Ag and Au better in the spectral range >600 nm, the Drude model is more accurate for large spheres, which have dipole resonances in that particular wavelength range [see Fig. 3(a)]. It can be concluded from Figs. 3 and 4 that for plasmon-enhanced luminescence at wavelengths below ~600 nm, Ag is more suitable than Au due to the smaller contributions of interband transitions to the imaginary part of the dielectric function. If electron-surface scattering is taken into account,[36] the decrease in quantum efficiency for particles smaller than ~20 nm is somewhat faster than shown in Fig. 3(b). The existence of an optimum diameter for quantum efficiency enhancement of a few tens of nanometers is, however, independent of electron-surface scattering.

In order to explain the origin of the optimal sphere diameter for quantum efficiency enhancement, as shown in Fig. 3(b), Fig. 5 illustrates the sphere-diameter dependencies of the two processes that determine the quantum efficiency enhancement. We consider the same parameters as were used in Fig. 3, and we limit ourselves to Ag. Figure 5(a) displays the contribution of the total excited state decay rate that is associated with coupling to the dipole plasmon mode $\Gamma_{TOT,DIP}$ versus sphere diameter (see the Appendix for an explanation on how this dipole contribution is determined). The wavelength corresponds to the wavelength displayed in Fig. 3(a). The decay rate increases in magnitude for decreasing diameter. This trend is qualitatively comparable to the mode-volume dependence of the emission rate enhancement of an atom that is coupled to an optical microcavity mode in the weak coupling regime. Within that context, emission rate enhancements are often described using the Purcell factor, which is inversely proportional to the mode volume.[37] A detailed analysis of the correspondence between decay rate modifications near a metal sphere and the Purcell factor (as, e.g., in Ref. 38) is beyond the scope of this paper.

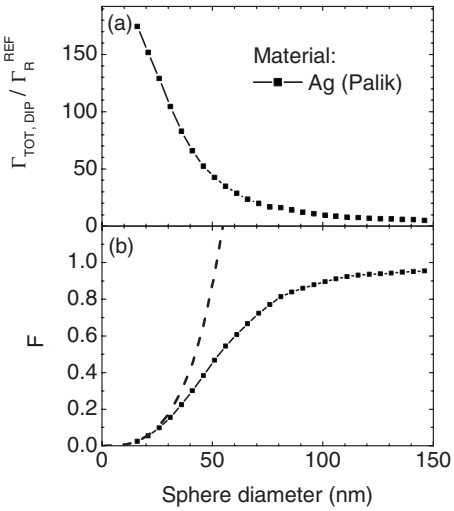

FIG. 5. (a) Contribution to the total excited state decay rate that is associated with coupling to the dipole plasmon mode of the Ag sphere $\Gamma_{TOT,DIP}$, normalized to the radiative decay rate in the absence of the sphere Γ_R^{REF}, versus sphere diameter. (b) Fraction of the energy coupled to the dipole plasmon mode that is reradiated F (line with symbols). The dashed line represents the albedo of the sphere according to the quasistatic theory. The data represented as lines with symbols are calculated from the exact electrodynamical theory. The parameters are the same as for Fig. 3, and the wavelength corresponds to the wavelength displayed in Fig. 3(a).

Figure 5(b) shows the fraction of the total power coupled to the dipole mode that is reradiated, denoted as F (line with symbols). This quantity, which is identical to the ratio of the dipolar components of the scattering and extinction cross sections, increases with diameter. Below a diameter of ~30 nm, F equals the albedo of a spherical Rayleigh scatterer (dashed line), which is proportional to diameter cubed. Above ~30 nm, F flattens off due to retardation effects.

Since quantum efficiency enhancement involves both effective coupling of the emitter to the plasmon mode and efficient outcoupling of plasmons into radiation, the opposite dependencies on sphere diameter shown in Figs. 5(a) and 5(b) give rise to a trade-off. This explains the origin of the optimal diameter for quantum efficiency enhancement.

B. Higher-order mode contributions to the emission enhancement

At wavelengths above ~600 nm, resonant plasmon modes can be obtained by increasing the particle size, as shown in Fig. 3(a). However, plasmon-enhanced luminescence is less effective for larger particles [see Fig. 3(b)]. An alternative strategy to achieve resonantly enhanced luminescence at larger wavelengths, but with small particles, is to use nonspherical particles, with redshifted longitudinal resonances,[39] to use arrays of coupled particles,[40] or to increase the refractive index of the embedding medium.[41]

Figure 6 illustrates the effect of a high-index embedding medium (n=3.5) on the quantum efficiency enhancement associated with coupling to the dipole mode of a sphere. Figure 6(a) shows that the higher refractive index causes a strong

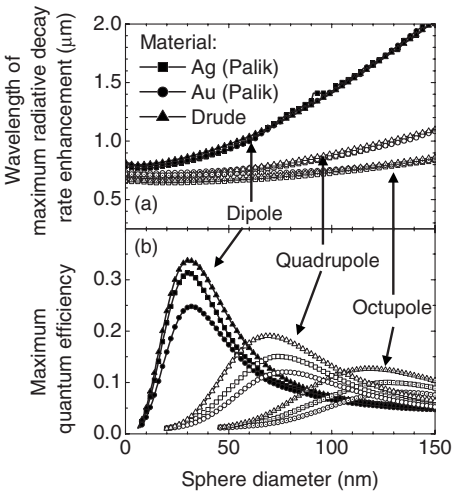

FIG. 6. Calculations for a dipole emitter, the orientation of which is averaged over all solid angles, positioned in close proximity to a metal sphere (see text), embedded in a medium with a refractive index of 3.5. (a) Wavelength of maximum radiative decay rate enhancement due to coupling to either the dipole mode (closed symbols), the quadrupole mode (open symbols), or the octupole mode (open symbols with dots) versus sphere diameter, plotted for three sphere materials: Ag, Au, and a Drude-model fit for Ag. (b) Maximum quantum efficiency versus sphere diameter at the wavelengths shown in (a) for the same three materials. The maximum quantum efficiency was found by varying the emitter-sphere separation (see text). The quantum efficiency of the emitter in the absence of the sphere is 1%. Calculation method: exact electrodynamical theory.

increase of the wavelength of maximum radiative decay rate enhancement (closed symbols) compared to the data shown in Fig. 3(a) for $n=1.3$. Resonance wavelengths as large as 2.0 μm are observed for 150-nm-diameter particles. Figure 6(b) shows the maximum quantum efficiency calculated at the wavelength of maximum radiative decay rate enhancement (closed symbols). The curves for the three materials are more similar to each other than in Fig. 3(b). We attribute this to a better correspondence between the dielectric functions of the three materials in the spectral range of interest (see Fig. 4). The maximum quantum efficiencies for Ag and Au reach values of up to 31% and 25%, respectively, for a diameter of about 30 nm. These enhancements are substantially higher than the values in Fig. 3(b), which confirms that plasmon-enhanced luminescence can be more effective for emission wavelengths above 600 nm, because interband transitions are prominent only below 600 nm.

In contrast to the trend for Ag and Au, the maximum quantum efficiency for the Drude metal is smaller in Fig. 6(b) than in Fig. 3(b): 34% versus 52%, at around 30 nm. This effect is attributed to the difference in frequency dependencies of dissipation and radiation of the energy that is coupled to the dipole plasmon mode. The dissipation rate hardly depends on frequency, since the electron relaxation rate is fixed in the Drude model (the frequency dependence only enters via the fraction of energy that is captured in the metal), whereas the local density of states of the embedding medium increases with the square of the transition frequency (and depends linearly on the refractive index of the medium). Consequently, plasmon-enhanced luminescence due to resonant coupling to plasmon modes of a Drude-metal sphere is more efficient at high emission frequencies. The smaller refractive index that is associated with the smaller resonance wavelength does not fully compensate this trend.

Figure 6(b) also shows quantum efficiency enhancement data obtained at the wavelengths of maximum radiative decay rate enhancement that are associated with coupling to either the quadrupole mode (open symbols) or the octupole mode (open symbols with dots). For the calculation of the maximum quantum efficiency, the contributions of all multipole modes at the wavelength of interest were taken into account for completeness. However, the radiative decay rate enhancement is dominated by the resonant mode in all cases. In Fig. 6(b), it is shown that, for spheres of about 75 nm, resonant coupling to the quadrupole mode can increase the quantum efficiency to 14% for Ag and to 11% for Au. The octupole mode enhances the quantum efficiency at diameters of around 130 nm, with slightly smaller maximum values as for coupling to the quadrupole mode. The quadrupole and octupole features in Fig. 6(b) illustrate that higher-order modes radiate rather efficiently for larger sphere sizes, which implies that they cannot be considered as dark modes for those sphere sizes. This issue is further discussed in Sec. V.

Since the quadrupole and octupole modes have smaller resonance wavelengths than the dipole mode, the associated maximum quantum efficiency enhancement occurs at a shorter wavelength, as shown in Fig. 6(a). Resonant coupling to higher-order modes is ineffective for increasing the quantum efficiency for spheres embedded in a medium with a refractive index of 1.3 (Fig. 3), as interband transitions increase dissipation too much in the corresponding spectral range.

V. GERSTEN AND NITZAN MODEL VERSUS EXACT ELECTRODYNAMICAL THEORY

All results in the previous sections were calculated from the exact electrodynamical theory. This section presents a comparison with the original and improved GN models, which are described in Sec. II. The advantage of the GN model is that it can be generalized to spheroids based on an orthogonal set of eigenfunctions, so that shape-induced shifts of the plasmon resonance frequencies and shape-induced changes in field intensities can be accounted for. Such an orthogonal set of eigenfunctions for a spheroid is not known for exact electrodynamical theory.[23]

A. Emission pattern

Figure 7 shows polar plots of the angular emission distribution of a source dipole located at a distance of 10 nm from the surface of a 60-nm-diameter Ag sphere, embedded in a medium with a refractive index of 1.3 for (a) the radial dipole orientation and (b) the tangential dipole orientation, both as indicated in the figure. The solid lines represent calculations by the exact electrodynamical theory, and the dashed lines represent the emission patterns associated with

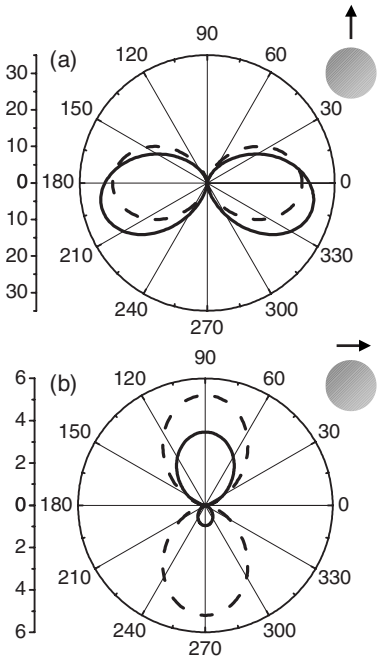

FIG. 7. Polar plots of the angular intensity distributions of a dipole source, embedded in a medium with a refractive index of 1.3, at a distance of 10 nm from a 60-nm-diameter Ag sphere for (a) the radial dipole orientation and (b) the tangential dipole orientation, as indicated next to the polar plots. The solid lines represent calculations by the exact electrodynamical theory; the dashed lines represent the emission patterns associated with the improved GN model. The patterns in both plots are normalized to the maximum value of the emission pattern of the same source dipole in the absence of the sphere. All patterns were calculated at the wavelength of maximum radiative decay rate enhancement: 433 nm for the exact electrodynamical theory and 449 nm for the improved GN model (see text).

the GN model. The latter patterns are implicitly assumed to be dipole patterns, as the emission properties of the coupled system are characterized with an effective dipole moment, as discussed in Sec. II. The emission patterns for both dipole orientations were obtained at a specifically chosen wavelength, i.e., the wavelength that corresponds to the maximum radiative decay rate enhancement for an isotropic dipole ensemble. The numerical values for this wavelength are slightly different for the two calculation methods: 433 nm for the exact electrodynamical theory and 449 nm for the improved GN model. Both graphs are normalized to the maximum value of the emission pattern of the same source dipole in the absence of the sphere.

Figure 7(a) shows that, for the radial dipole orientation, the emission patterns are roughly similar in terms of shape and magnitude for both methods. The integral of the emission pattern over all solid angles, i.e., the radiative decay rate, is found to be 28 times larger than that of the same dipole emitter in the absence of the sphere, when calculated from the exact electrodynamical theory, and 26 times larger, when calculated from the GN model. In contrast, Fig. 7(b) shows that the emission patterns for the two methods are very different for the tangential dipole orientation. The deviation from the dipole emission pattern that is obtained from the exact electrodynamical theory is a consequence of interference between the source dipole, the induced dipole and induced higher-order multipoles. This interference phenomenon is not described by the GN model due to its intrinsic restriction to dipole emission patterns. As a consequence, the calculated radiative decay rate enhancements for the tangential dipole orientation are rather different for the two methods: a factor of 2.2 for the exact electrodynamical theory and a factor of 5.2 for the GN model. The fact that the emission pattern for the radial orientation resembles the dipole pattern much better than for the tangential orientation can be partly attributed to the fact that the radial dipole configuration is rotationally symmetric, as the dipole itself, in contrast to the tangential dipole configuration. Highly structured emission patterns of an atom near an absorbing sphere have been analyzed by Dung *et al.*[42]

For both models, the radiative decay rate enhancements for the radial orientation are substantially different from the radiative decay rate enhancements for the orientation tangential to the sphere surface. This feature is of great importance for designing optimized metal-emitter geometries. The orientation-dependent behavior of the radiative decay rate enhancement is further discussed in Figs. 9 and 10.

B. Emission enhancement

Figure 8 shows a comparison between the distance dependencies of the decay rate modifications obtained by the original (dashed lines) and improved (solid lines) GN models and by the exact electrodynamical theory (symbols). As in Fig. 1, a Ag sphere with a diameter of 60 nm is considered. Figure 8(a) shows that the radiative decay rate versus separation obtained with the improved GN model resembles the exact result significantly better than the curve obtained from the original GN model. The latter method leads to a substantial overestimation of the radiative decay rate. Figures 8(b) and 8(c) show similar effects for both nonradiative decay rate and quantum efficiency versus separation. We conclude from Fig. 8 that the improved GN model provides a fairly accurate description of the decay rate modifications associated with resonant coupling to the dipole mode of a 60-nm-diameter Ag sphere, despite the large differences shown in Fig. 7(b). This is due to the fact that the largest contribution to the orientation-averaged enhancement is associated with the radial dipole orientation for which the improved GN model and the exact theory yield quite similar radiation patterns. In addition, the slightly smaller radiative decay rate enhancement for the radial orientation (factor 26 vs 28 at 10 nm separation), as calculated from the improved GN model, is counterbalanced by the larger enhancement for the tangential orientation (factor 5.2 vs 2.2 at 10 nm separation).

Figures 7 and 8 focus on a 60-nm-diameter Ag sphere. In order to extend the comparison between the models to a larger sphere-diameter range, Fig. 9 shows the dependence of the maximum quantum efficiency on sphere diameter, analogous to Fig. 3, calculated from the original (dashed lines) and improved (solid lines) GN models and by the exact electrodynamical theory (symbols). Figure 9(a) displays the wavelength of maximum radiative decay rate enhancement

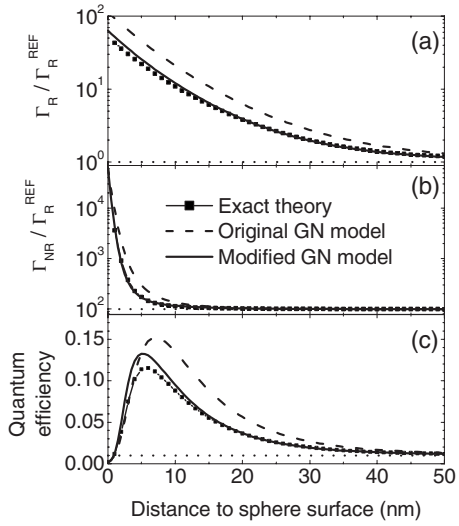

FIG. 8. Comparison of the distance-dependent modifications of the radiative and nonradiative decay rates as well as of the quantum efficiency, as obtained by the original (dashed lines) and improved (solid lines) GN models and by the exact electrodynamical theory (symbols). (a) Radiative decay rate of a dipole emitter, the orientation of which is averaged over all solid angles, versus the distance to the surface of a 60-nm-diameter Ag sphere, and the radiative decay rate in the absence of the sphere (dotted line). (b) Nonradiative decay rate versus distance to the sphere surface, and the nonradiative decay rate in the absence of the sphere (dotted line). The decay rates in both (a) and (b) are normalized to the radiative decay rate in the absence of the sphere. (c) Quantum efficiency versus distance to the sphere surface and the quantum efficiency in the absence of the sphere (dotted line). All curves were calculated at the wavelength of maximum radiative decay rate enhancement: 433 nm for the exact electrodynamical theory, 394 nm for the original GN model, and 449 nm for the improved GN model. The data obtained with the exact electrodynamical theory are identical to the data shown in Fig. 1.

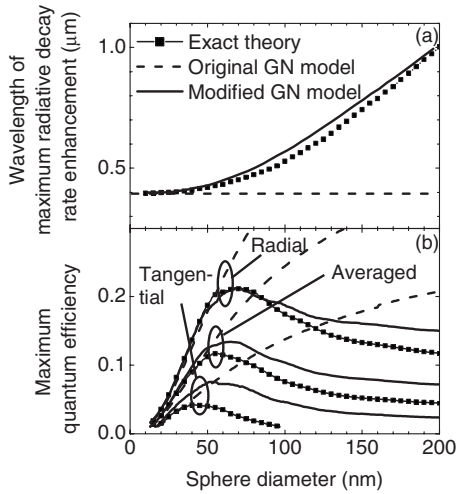

FIG. 9. (a) Wavelength of maximum radiative decay rate enhancement associated with coupling to the dipole plasmon mode versus sphere diameter, for a dipole emitter positioned in close proximity to a Ag sphere. The orientation of the dipole is averaged over all solid angles. (b) Maximum quantum efficiency versus sphere diameter at the wavelength of maximum radiative decay rate enhancement shown in (a) for three dipole emitter orientations: radial, tangential, and averaged over all solid angles. In both graphs, results obtained with the original GN model (dashed lines), the improved GN model (solid lines), and the exact electrodynamical theory (lines with symbols) are plotted. The refractive index of the embedding medium is 1.3 and the quantum efficiency of the emitter in the absence of the sphere is 1%. The data for the dipole orientation averaged over all solid angles obtained with the exact electrodynamical theory are identical to the data for Ag shown in Fig. 3.

versus sphere diameter for a dipole emitter positioned in close proximity to a Ag sphere, for a dipole orientation that is averaged over all solid angles. Only a small difference is found between the improved GN model and the exact theory over the whole diameter range, whereas the result from the original GN model, which does not describe the redshift of the dipole plasmon mode with increasing diameter, is entirely incorrect at larger sphere sizes. This confirms that the well-known corrections introduced by Wokaun and coworkers.[24,25] provide a substantial improvement to the quasistatic description in the particle-size range of interest.

Figure 9(b) shows the maximum quantum efficiency of the dipole emitter versus sphere diameter calculated at the wavelengths shown in Fig. 9(a) for (1) the radial dipole orientation, (2) the tangential dipole orientation, and (3) the orientation averaged over all solid angles. For all three cases, the underlying optimal emitter-sphere separation (as in Fig. 2) is in the range between 3 and 10 nm. Most notably, the original GN model does not describe the decrease in quantum efficiency enhancement for larger sphere sizes, as is obtained from the exact electrodynamical theory. In contrast, the improved GN model does describe this characteristic behavior. This difference illustrates an important advantage of the improved GN model compared to the original version.

When comparing the improved GN model to the exact electrodynamical theory in more detail, perfect agreement is observed for the radial dipole orientation up to a diameter of 90 nm. For the orientation tangential to the surface, the two methods start to deviate at a diameter as small as 30 nm, consistent with what was found in Fig. 7 for the 60-nm-diameter sphere. For the dipole orientation averaged over all solid angles, the maximum quantum efficiency enhancement, as calculated from the improved GN model, deviates by 5% (i.e., 6.2% instead of 5.9%) from the exact result for a diameter of 30 nm, 15% for a diameter of 60 nm, and 35% for a diameter of 100 nm. These numbers indicate the applicability of the GN model, with the corrections for radiation damping and dynamic depolarization included, when applied to larger particles.

Figures 7 and 9 show that, at the wavelength under investigation, the radiative decay rate enhancement for the radial dipole orientation is substantially higher than for the tangential dipole orientation. To examine the difference between the two orientations in more detail, Fig. 10 shows the spectral dependence of the radiative decay rate enhancement for the radial and tangential dipole orientations. The separation is fixed at 10 nm, and the refractive index of the embedding medium is 1.3. Two sphere diameters are considered: 30 nm in Fig. 10(a) and 60 nm in Fig. 10(b). The results are plotted

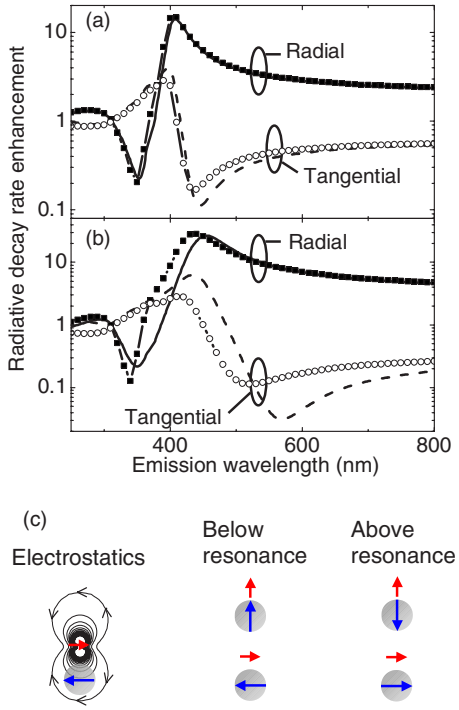

FIG. 10. (Color online) [(a) and (b)] Radiative decay rate enhancement, on a logarithmic scale, versus emission wavelength for a dipole emitter at a distance of 10 nm from the surface of a Ag sphere embedded in a medium with a refractive index of 1.3, for two dipole orientations: radial and tangential. The sphere diameter is 30 nm in (a) and 60 nm in (b). Results obtained with both the exact electrodynamical theory (symbols) and with the improved GN model (lines) are plotted. (c) Illustration of a source dipole in red (dark gray) that induces a dipole in the sphere in the electrostatic limit, shown in blue (black), together with the configurations of source and induced dipoles for source dipole frequencies far below and far above the dipole resonance of the sphere.

both for the exact electrodynamical theory (symbols) and the improved GN model (lines).

Figure 10(a) shows that, for a sphere diameter of 30 nm, the correspondence between the enhancement spectra obtained with both calculation methods is reasonably good for the tangential dipole orientation and very good for the radial orientation. The agreement between both methods again confirms the applicability of the improved GN model to particles of this size. Figure 10(b) illustrates that when the sphere diameter is increased, the agreement between the improved GN model and the exact electrodynamical theory diminishes.

C. Spectral trends in emission enhancement

Apart from the comparison between the two methods, Fig. 10(a) also provides a spectral comparison between the two dipole orientations. The enhancement spectra for both orientations are found to exhibit dispersive lineshapes characteristic of electromagnetic resonances. We relate the dispersive lineshape to the fact that the driving field in the sphere has an orientation relative to the source dipole that depends on the source dipole orientation relative to the sphere: either the

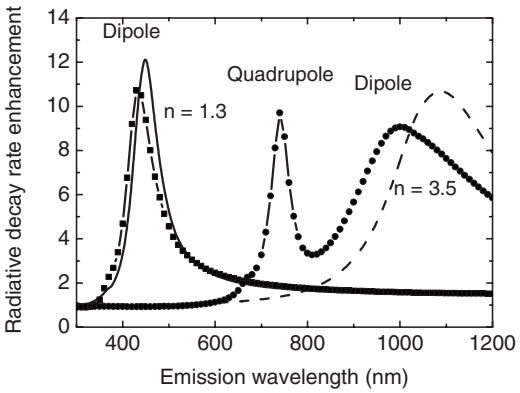

FIG. 11. Radiative decay rate enhancement versus emission wavelength for a dipole emitter, the orientation of which is averaged over all solid angles, at a distance of 10 nm from the surface of a 60-nm-diameter Ag sphere embedded in a medium with either a refractive index of 1.3 (square symbols and solid line) or a refractive index of 3.5 (round symbols and dashed line), both calculated from the exact electrodynamical (symbols) and improved (lines) GN models.

driving field is mainly parallel to the source dipole (for the radial dipole orientation) or mainly antiparallel (for the tangential dipole orientation). Since the phase of the induced dipole in the sphere exhibits a 180° phase shift with respect to the driving field at the resonance frequency,[43] the source dipole and the induced dipole interfere destructively below the resonance frequency (for the tangential dipole orientation) or above the resonance frequency (for the radial dipole orientation). These configurations of source dipole and induced dipole are schematically depicted in Fig. 10(c). Since destructive interference is associated with a reduction of the radiative decay rate, the dip in the radiative decay rate enhancement [see Fig. 10(a)] is either visible at emission wavelengths smaller than the dipole resonance wavelength (for the radial dipole orientation) or at wavelengths larger than the dipole resonance wavelength (for the tangential dipole orientation).

The fact that the peak enhancement in Fig. 10(a) is different for the radiative decay rate enhancement for the two dipole orientations can be partly attributed to the fact that the near field of a dipole is twice as strong along the dipole direction as in the perpendicular direction (for the same distance). As a consequence, a dipole that is oriented radially induces a stronger dipole in the sphere than a dipole that is oriented tangentially to the sphere surface.

D. Higher-order mode contributions to the emission enhancement

A specific aspect of the decreasing agreement between the GN model and the exact electrodynamical theory for larger spheres is illustrated in Fig. 11, which shows the radiative decay rate enhancement versus emission wavelength for two refractive indices of the embedding medium: 1.3 and 3.5. The calculations were done with the exact electrodynamical theory (symbols) and with the improved GN model (lines).

The figure shows that the spectral features associated with coupling to the dipole mode are very similar for both calculation methods. The peaks obtained by the improved GN model have slightly higher maximum values and are centered at slightly larger wavelengths, which correspond to the trend shown in Fig. 9. In addition to the features that are associated with coupling to the dipole mode, the exact electrodynamical theory shows a peak at 740 nm, for the refractive index of 3.5, which is due to coupling to the quadrupole mode. This contribution is absent in the spectrum that is obtained with the improved GN model due to the fact that this model is based on the assumption that higher-order modes are dark modes, which is only correct for particles that are much smaller than the wavelength of light. With the high refractive index, and hence short wavelength in the embedding medium, this condition is not fulfilled. Indeed, it appears that quadrupole modes are interesting alternatives to dipole modes for emission enhancement. They provide additional wavelength tunability and narrower spectra.

VI. CONCLUSIONS

We have used an exact electrodynamical theory to investigate modifications of the radiative and nonradiative decay rates of a dipole emitter by resonant coupling to the plasmon modes of a metal sphere at short distance. The study focused on enhancing the quantum efficiency of a low-quantum-efficiency emitter in order to elucidate some important aspects of plasmon-enhanced luminescence.

It has been shown that characteristic features, such as the subsequent enhancement and reduction of the quantum efficiency upon decreasing the emitter-sphere separation, can be described based entirely on a local electromagnetic response, which involves coupling to both radiative and dark plasmon modes (see Fig. 1). The magnitude of the quantum efficiency enhancement is found to strongly depend on sphere diameter. This effect can be described based on the electromagnetic properties of the radiative dipole mode only, without invoking coupling to dark multipole modes (see Fig. 2). In particular, the optimal diameter is found to originate from the trade-off between (1) the coupling strength of an emitter with a plasmon mode, which is highest for small spheres [see Fig. 5(a)], and (2) the efficiency with which that plasmon mode couples to the far field, which is maximal for large spheres [see Fig. 5(b)].

The optimal sphere diameter for luminescence quantum efficiency enhancement depends both on the metal and on the embedding medium (see Figs. 3 and 6). Very small spheres (<10 nm) are ineffective for plasmon-enhanced luminescence for all metals, including the ideal Drude metal. For an embedding medium with a refractive index of 1.3, the optimal sphere diameter is 55 nm for Ag, 110 nm for Au, and 30 nm for the ideal Drude metal (see Fig. 3). The large spread in optimal diameters is related to the different contributions of interband transitions for Ag and Au at wavelengths below 600 nm (see Fig. 4). For an embedding medium with a refractive index of 3.5, which results in dipole resonances away from the interband transitions, the optimal diameter is around 30 nm for all three metals (see Fig. 6). At this diameter, the quantum efficiency of the emitter is increased from 1% to over 30% for the Ag sphere.

Resonant coupling to higher-order modes may increase the quantum efficiency of an emitter as well, but only for larger diameters (see Fig. 6). The maximum quantum efficiency enhancement due to coupling with higher-order modes, however, does not reach the value obtained for coupling to the dipole mode.

In order to correlate the sphere-size dependence of plasmon-enhanced luminescence with the properties of individual plasmon modes, the presented analysis has been performed for a variable, optimized emission wavelength (see Figs. 3 and 6). If the emission of an atom or quantum dot with a fixed emission wavelength needs to be optimized, this approach is of limited value. Besides particle size, it is, however, also possible to tune particle shape, which would enable the optimization of the particle geometry for a given dipole resonance wavelength. Since the coupling of an emitter with a nonspherical particle cannot be calculated analytically from the exact electrodynamical theory, the GN model could be an appropriate alternative. Within that context, we have verified the applicability of the GN model to finite-sized particles by comparing this model to the exact electrodynamical theory for the sphere geometry.

The GN model, which is improved to include well-known corrections for radiative damping and dynamic depolarization, provides reasonably accurate results for the decay rate modifications that are due to coupling to the dipole plasmon mode, both spatially (Fig. 8) and spectrally (Fig. 10), if the particles are small. The improved GN model is applicable over a substantially larger size range than the original GN model and does describe the existence of a finite optimal diameter for plasmon-enhanced luminescence (see Fig. 9). Without the corrections, the GN model does not describe the existence of such an optimal diameter and deviates considerably from the results obtained from the exact electrodynamical theory. For the radial dipole orientation, the agreement is found to be substantially better than for the tangential dipole orientation, which can be partly attributed to the rotational symmetry for the radial dipole orientation, which is absent for the tangential orientation.

Two features that are not well described by the improved GN model are the angular redistribution of emission by coupling to plasmon modes (Fig. 7) and the enhancement of the radiative decay rate due to coupling to higher-order plasmon modes (Figs. 6 and 11). These limitations leave unaffected that the improved GN model is a powerful tool for describing trends associated with plasmon-enhanced luminescence, not only for spheres but also for spheroids. The applicability to spheroids enables the investigation of the influence of shape anisotropy on plasmon-enhanced luminescence in an analytical way.

ACKNOWLEDGMENTS

This work is part of the research program of the "Stichting voor Fundamenteel Onderzoek der Materie (FOM)," which is financially supported by the "Nederlandse organisatie voor Wetenschappelijk Onderzoek (NWO)." This work

was also partially supported by NANONED, a nanotechnology program of the Dutch Ministry of Economic Affairs, and by AFOSR MURI Award No. FA9550-05-1-0450.

APPENDIX: EXPRESSIONS FOR THE DECAY RATES OF AN ATOM IN THE PRESENCE OF A SPHERE ACCORDING TO THE EXACT ELECTRODYNAMICAL THEORY

This appendix lists the expressions for the total decay rate Γ_{TOT} and the radiative decay rate Γ_R of an excited atom in close proximity to a sphere, as obtained from the exact electrodynamical theory.[19]

The atom, which is modeled as a classical dipole with dipole moment μ, is positioned at a distance d from the surface of a sphere with radius a and dielectric constant $\varepsilon = \varepsilon' + i\varepsilon''$. We consider two dipole orientations: radial and tangential. For the radial dipole orientation, i.e., perpendicular ($\perp$) to the sphere surface, we obtain

$$\frac{\Gamma_{\mathrm{TOT}}^{\perp}}{\Gamma_R^{\mathrm{REF}}} = 1 + \frac{3}{2}\,\mathrm{Re}\sum_{l=1}^{\infty}(2l+1)l(l+1)b_l\left[\frac{h_l^{(1)}(kr)}{kr}\right]^2, \tag{A1}$$

$$\frac{\Gamma_R^{\perp}}{\Gamma_R^{\mathrm{REF}}} = \frac{3}{2}\sum_{l=1}^{\infty}(2l+1)l(l+1)\left|\frac{j_l(kr)+b_l h_l^{(1)}(kr)}{kr}\right|^2, \tag{A2}$$

and for the tangential dipole orientation, i.e., parallel ($\parallel$) to the sphere surface:

$$\frac{\Gamma_{\mathrm{TOT}}^{\parallel}}{\Gamma_R^{\mathrm{REF}}} = 1 + \frac{3}{2}\,\mathrm{Re}\sum_{l=1}^{\infty}\left(l+\frac{1}{2}\right)\left\{b_l\left[\frac{\zeta_l'(kr)}{kr}\right]^2 + a_l[h_l^{(1)}(kr)]^2\right\}, \tag{A3}$$

$$\frac{\Gamma_R^{\parallel}}{\Gamma_R^{\mathrm{REF}}} = \frac{3}{4}\sum_{l=1}^{\infty}(2l+1)\left[|j_l(kr)+a_l h_l^{(1)}(kr)|^2 + \left|\frac{\psi_l'(kr)+b_l\zeta_l'(kr)}{kr}\right|^2\right], \tag{A4}$$

where Γ_R^{REF} refers to the radiative decay rate for the dipole located in the embedding (nonabsorbing) medium in the absence of the sphere, j_n and $h_n^{(1)}$ are the ordinary spherical Bessel and Hankel functions, $\psi_n(x) \equiv x j_n(x)$, $\zeta_n(x) \equiv x h_n^{(1)}(x)$, a_n and b_n are the Mie scattering coefficients of the sphere, $r = a + d$, $k = \sqrt{\varepsilon_m}\omega/c$, ε_m is the dielectric constant of the embedding medium, ω the optical frequency (in rad/s), c the speed of light in vacuum, and l is the angular mode number. The derivatives of ψ_n and ζ_n are derivatives to kr. Both $\Gamma_{\mathrm{TOT}}^{\perp}$ and $\Gamma_{\mathrm{TOT}}^{\parallel}$ refer to the total decay rate of an emitter with a luminescence quantum efficiency of 100% in the absence of the sphere.

In the paper, we have considered Γ_{TOT} and Γ_R not only for the radial and tangential orientations, but also for the orientation that is averaged over all solid angles. The decay rates for the latter configuration are calculated by averaging the results for the radial and tangential orientations (with a weight factor for the tangential orientation that is twice the weight factor for the radial orientation). We have numerically verified, based on Ref. 20, that this approach is correct despite the fact that the radiative decay rate for a specific dipole orientation does not depend linearly on the Mie scattering coefficients [see Eqs. (A2) and (A4)], in contrast to the total decay rate [see Eqs. (A1) and (A3)].

In addition, we have decomposed the radiative and nonradiative decay rates in contributions associated with different plasmon modes. Each contribution is calculated from Eqs. (A1)–(A4) by first taking all Mie scattering coefficients, except the ones associated with the mode under investigation, to be zero. Second, the free-space contribution (=1), which is independent of any Mie scattering coefficient, is subtracted. Note that for the radiative decay rate, the summation does still need to be carried out over a large range of angular mode numbers l in order to describe the free-space contribution correctly.

The decomposition of the decay rates into contributions associated with the coupling to different plasmon modes is somewhat artificial as individual contributions to the radiative decay rate can yield negative values. However, this approach does facilitate the visualization of the distinct influence of different plasmon modes on phenomena such as quenching at short emitter-metal distances and the determination of the maximum quantum efficiency (see Figs. 1 and 2). Also the calculation of the wavelength of maximum radiative decay rate enhancement that is associated with a particular mode, as shown in Figs. 3(a), 6(a), and 8(a), relies on the decomposition of the radiative decay rate into mode-specific contributions. Note that the calculations of the maximum quantum efficiency, as shown in Figs. 3(b), 6(b), and 8(b), do not rely on this procedure.

*mertens@amolf.nl

[1] R. M. Amos and W. L. Barnes, Phys. Rev. B **55**, 7249 (1997).
[2] E. Dulkeith *et al.*, Phys. Rev. Lett. **89**, 203002 (2002).
[3] J. N. Farahani, D. W. Pohl, H.-J. Eisler, and B. Hecht, Phys. Rev. Lett. **95**, 017402 (2005).
[4] P. Anger, P. Bharadwaj, and L. Novotny, Phys. Rev. Lett. **96**, 113002 (2006).
[5] S. Kühn, U. Håkanson, L. Rogobete, and V. Sandoghdar, Phys. Rev. Lett. **97**, 017402 (2006).
[6] P. Mühlschlegel, H.-J. Eisler, B. Hecht, and D. W. Pohl, Science **308**, 1607 (2005).
[7] V. A. Podolskiy, A. K. Sarychev, Narimanov, and V. M. Shalaev, Proceedings of the Annual APS/URSI Meeting (APS) 2004 (unpublished), Vol. 2, p. 1915.
[8] J. S. Biteen, N. S. Lewis, H. A. Atwater, H. Mertens, and A. Polman, Appl. Phys. Lett. **88**, 131109 (2006).

[9] H. Mertens and A. Polman, Appl. Phys. Lett. **89**, 211107 (2006).
[10] H. Mertens, H. A. Atwater, J. S. Biteen, and A. Polman, Nano Lett. **6**, 2622 (2006).
[11] J. R. Lakowicz, Plasmonics **1**, 5 (2006).
[12] L. Novotny, Appl. Phys. Lett. **69**, 3806 (1996).
[13] V. V. Klimov, M. Ducloy, and V. S. Letokhov, Eur. Phys. J. D **20**, 133 (2002).
[14] H. T. Dung, L. Knöll, and D. G. Welsch, Phys. Rev. A **62**, 053804 (2000).
[15] L. Rogobete and C. Henkel, Phys. Rev. A **70**, 063815 (2004).
[16] L. A. Blanco and F. J. García de Abajo, Phys. Rev. B **69**, 205414 (2004).
[17] R. Carminati, J.-J. Greffet, C. Henkel, and J. M. Vigoureux, Opt. Commun. **261**, 368 (2006).
[18] R. Ruppin, J. Chem. Phys. **76**, 1681 (1982).
[19] Y. S. Kim, P. T. Leung, and T. F. George, Surf. Sci. **195**, 1 (1988).
[20] C.-T. Tai, *Dyadic Green Functions in Electromagnetic Theory*, 2nd ed. (IEEE, New York, 1993).
[21] J. Gersten and A. Nitzan, J. Chem. Phys. **75**, 1139 (1981), Sec. II.
[22] For a detailed mathematical appendix of Ref. 21, see AIP Document No. PAPS JCP SA-75-1139-32, Sec. B.
[23] L.-W. Li, M.-S. Leong, P.-S. Kooi, and T.-S. Yeo, IEEE Trans. Antennas Propag. **49**, 645 (2001).
[24] A. Wokaun, J. P. Gordon, and P. F. Liao, Phys. Rev. Lett. **48**, 957 (1982).
[25] M. Meier and A. Wokaun, Opt. Lett. **8**, 581 (1983).
[26] K. L. Kelly, T. R. Jensen, A. A. Lazarides, and G. C. Schatz, in *Metal Nanoparticles: Synthesis, Characterization and Applications*, edited by D. Feldheim and C. Foss (Dekker, New York, 2002), p. 89.
[27] P. T. Leung, Y. S. Kim, and T. F. George, J. Phys. Chem. **92**, 6206 (1988).
[28] An online program to evaluate decay rate modifications near spherical and spheroidal nanoparticles is available on our website www.erbium.nl.
[29] E. M. Purcell, Phys. Rev. **69**, 681 (1946); Y. Xu, R. K. Lee, and A. Yariv, Phys. Rev. A **61**, 033807 (2000).
[30] R. R. Chance, A. Prock, and R. Silbey, Adv. Chem. Phys. **37**, 1 (1978).
[31] H. A. Haus and J. R. Melcher, *Electromagnetic Fields and Energy* (Prentice-Hall, Englewood Cliffs, NJ, 1989).
[32] D. J. Griffiths, *Introduction to Electrodynamics* (Prentice-Hall, Upper Saddle River, NJ, 1999).
[33] K. L. Kelly, E. Coronado, L. L. Zhao, and G. C. Schatz, J. Phys. Chem. B **107**, 668 (2003).
[34] E. D. Palik, *Handbook of Optical Constants of Solids* (Academic, Orlando, FL, 1985).
[35] M. I. Stockman, S. V. Faleev, and D. J. Bergman, Phys. Rev. Lett. **87**, 167401 (2001).
[36] U. Kreibig and M. Vollmer, *Optical Properties of Metal Clusters* (Springer, Berlin, 1995).
[37] K. Vahala, Nature (London) **424**, 839 (2003).
[38] S. A. Maier, Opt. Express **14**, 1957 (2006).
[39] T. R. Jensen, M. D. Malinsky, C. L. Haynes, and R. P. Van Duyne, J. Phys. Chem. B **104**, 10549 (2000).
[40] M. Quinten and U. Kreibig, Appl. Opt. **32**, 6173 (1993).
[41] D. D. Nolte, J. Appl. Phys. **76**, 3740 (1994).
[42] H. T. Dung, L. Knöll, and D.-G. Welsch, Phys. Rev. A **64**, 013804 (2001).
[43] C. Bohren and D. Huffman, *Absorption and Scattering of Light by Small Particles* (Wiley, New York, 1983).